



# Regulating Cu atom orbital state on self-built photogate catalyst for improving HCOOH selectivity of CO<sub>2</sub> reduction

Jin Ming Wang<sup>a</sup>, Jeong Heon Lee<sup>a</sup>, Je Hee Lee<sup>a</sup>, Tae Gyun Woo<sup>a</sup>, Yue Xing Zhang<sup>b</sup>,  
Woo Dong Jang<sup>a,\*</sup>, Tae Kyu Kim<sup>a,\*</sup>

<sup>a</sup> Department of Chemistry, Yonsei University, Seoul 03722, South Korea

<sup>b</sup> College of Chemistry and Chemical Engineering, Hubei University, Wuhan 430072, China

## ARTICLE INFO

### Keywords:

Atom site catalysts  
Covalent organic frameworks  
CO<sub>2</sub> reduction  
Photogate molecular device

## ABSTRACT

While single atom site catalysts receive tremendous attention for CO<sub>2</sub> reduction, the understanding of orbital coupling interaction between metal-atom and CO<sub>2</sub> molecular remains challenging and rare toward CO<sub>2</sub> activation and selectivity of reduction products. Herein, binuclear-site Zn/Cu-porphyrin covalent organic framework (ZnCu-COF) photogate catalyst was synthesized, with characterizations of intraskeletal photogate molecular device (PMD). The ZnCu-COF showed the HCOOH selectivity of 89.1%, which was superior than Zn-COF and Cu-COF counterparts. The in-depth experimental and theoretical analyses reveal that Cu atom centers can enrich the electrons of Zn photocenters via directional and stepwise electron diffusion, which remarkably affects the orbital energy of Cu-3d, further deciding the electron state re-distribution of Cu-3d ( $d_{xy}$ ,  $d_{yz}$ ,  $d_{zx}$ ,  $d_{z^2}$ , and  $d_{x^2-y^2}$ ) orbitals. By a strong orbital coupling strength between Cu-3d<sub>z<sup>2</sup></sub> and C-2p<sub>z</sub>, Cu atom centers promote CO<sub>2</sub> activation and nucleophilic reaction of the unsaturated carbon of \*COOH intermediate, which clearly accounts for the different HCOOH and CO selectivity in COFs. This work opens critical perspective to the rational engineering, catalytic mechanism, and application of PMD-derived atomic-site catalysts.

## 1. Introduction

Photocatalytic CO<sub>2</sub> neutralization, for producing valuable chemical fuels, is considered an alternative environment-friendly solution for energy storage and alleviating atmospheric CO<sub>2</sub> levels [1,2]. The sluggish multiple-electron kinetics of CO<sub>2</sub> reduction reaction (CO<sub>2</sub>RR) become the primary bottleneck for artificial photosynthesis CO<sub>2</sub> fixation, and therefore, understanding the electron transfer pathways and identifying the active sites of CO<sub>2</sub>RR are highly instructive for developing efficient and robust photocatalysts [3–6]. Tremendous descriptors have been proposed for developing various photosystems to modulate the activity of catalytic centers [7,8], light-harvesting ability of chromophores [9,10], and efficiency of charge transfer between photosensitizers and catalytic centers [11,12]. Among which, intraskeletal photogate molecular device (PMD)-derived catalysts are recognized as promising candidates that integrate chromophoric photosensitizers, catalytic sites, and electron-transfer mediators to form a full-component molecular photosystem [13–17]. However, the majority of these molecular catalysts reported for light-driven CO<sub>2</sub>RR merely worked in

homogeneous systems, resulting in various conundrums for large-scale applications, including solvent-dependence solubility [18], unsatisfactory quantum efficiency [19,20], and vulnerability under harsh photocatalytic conditions [21].

Taking for a new class of crystalline porous materials, covalent organic frameworks (COFs), bridged by molecular organic units, have been developed as heterogeneous photocatalysts for CO<sub>2</sub>RR with merits of structural regularity, synthetic tunability, and high stability. Recently, various photosensitizers and catalytic sites have been complexed into COFs as inorganic nodes [22–24], organic linkers [25–27], or guests [28,29] for CO<sub>2</sub> photofixation. For example, by utilizing free Ru(bpy)<sub>3</sub><sup>2+</sup> as the photosensitizer, ultrathin COF-367-Co nanosheets were subject to heterogeneous photocatalysis for excellent CO<sub>2</sub>-to-CO conversion [29]. Cu/Ni nanoparticles were encapsulated into the pores of porphyrinic triazine framework [30]. These COF-based composite catalysts showed a good photoreduction CO<sub>2</sub> activity as a result of promoted electron separation and light absorption. However, the photoactive and catalytic centers in COFs are isolated in space, and long-distance electron migration is challenging owing to a weak

\* Corresponding authors.

E-mail addresses: [wjdjang@yonsei.ac.kr](mailto:wjdjang@yonsei.ac.kr) (W.D. Jang), [tkkim@yonsei.ac.kr](mailto:tkkim@yonsei.ac.kr) (T.K. Kim).

<https://doi.org/10.1016/j.apcatb.2022.122287>

Received 21 July 2022; Received in revised form 28 October 2022; Accepted 11 December 2022

Available online 15 December 2022

0926-3373/© 2022 Elsevier B.V. All rights reserved.

electronic coupling. To overcome these problems, an alternative strategy is to integrate close-lying PMDs into COF matrices that allow intraskeletal electron transfers between the directly bonded photosensitizers and catalytic centers at the COF compartments, facilitating an efficient energy transfer and electron diffusion during the CO<sub>2</sub>RR photocatalysis. Nevertheless, this type of bimetallic COF photocatalyst, inheriting distinctive photocatalytic features of homogeneous molecular catalysts, has been rarely explored to date.

As light-harvesting centers in natural photosynthesis, porphyrin derivatives have potential application in the fields of photocatalysis and photovoltaic conversion [31–33], owing to an impressive extinction coefficient in the blue-green light region and adjustable energy levels. Moreover, diverse meso/ortho-position substitutions can finely optimize the physicochemical and electrochemical properties [34–36], and variable metal ions can be incorporated into square-planar macrocycles serving as single-atom sites [37,38]. These significant advantages provide the motivation for designing PMD-type porphyrin-derived COFs, unifying multiple photosensitizing and catalytic units into COF system for heterogeneous CO<sub>2</sub>RR. We conjecture that integrating such porphyrin PMDs into COF networks could not only impart its distinctive photocatalytic features, but also provide a constructive strategy to heterogenize the PMDs for heterogeneous CO<sub>2</sub>RR under different condition. In addition, a deep insight into the selective mechanism to reveal the unique advantage of PMD-type COFs is highly desired, which is of great significance for the rational design of COF photocatalysts via structural and spatial isomerization.

With the above in mind, AB-stacked dual-site ZnCu-COF nanosheets (NSs) were fabricated by self-assembling Zn/Cu-porphyrin cores for photocatalytic CO<sub>2</sub>RR (Scheme S1). In these NSs, every Zn-porphyrin photoresponsive center is surrounded by four Cu-porphyrin catalytic units forming a highly-ordered square structure that facilitates PMD-type energy transfer and electron collection pathways (Scheme 1). For comparison, metal-deficient COF counterparts (Zn-COF and Cu-COF) were also synthesized for exploring the role of metal centers in influencing the PMD electrons during the photocatalytic process. The ultra-thin structure and high crystallinity of ZnCu-COF facilitates visualization of pore channels and individual building compartments through aberration-corrected scanning transmission electron techniques. The experimental and theoretical calculation results demonstrate that the Zn centers of the ZnCu-COF can modulate the orbital energy of Cu-3d ( $d_{xy}$ ,  $d_{yz}$ ,  $d_{zx}$ ,  $d_{z^2}$ , and  $d_{x^2-y^2}$ ) on Cu centers, by an efficient intraskeletal PMD electron transfer from Zn to Cu atom site under light irradiation, which affords significantly higher activity and selectivity of CO<sub>2</sub> reduction to HCOOH, and lower selectivity to CO.

## 2. Materials and methods

All analytical-grade raw materials (pyrrole, trifluoroacetic acid, 4-[(trimethylsilyl)ethynyl]benzaldehyde, pentafluorobenzaldehyde, p-bromobenzaldehyde, triphenylphosphine, Pd (II) acetate, and cuprous iodide) were purchased from Daejung Chemicals (Korea) and directly used without further purification. 5,15-bis(pentafluorophenyl)-10,20-bis(4-ethynylphenyl) porphyrin (FPP) [39,40] and 5,10,15,20-Tetrakis(4-bromophenyl) porphyrin (BPP) [41–43] was synthesized according to literature reported methods.

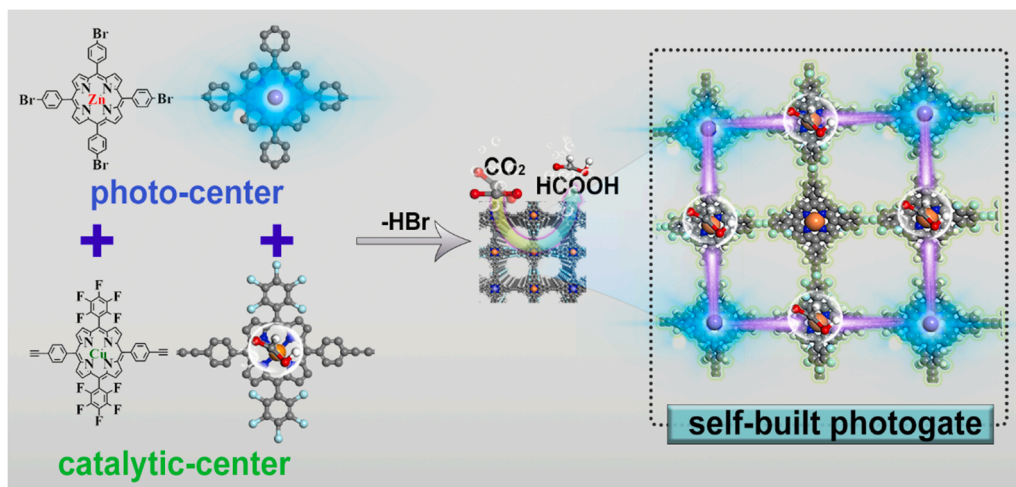
### 2.1. Material preparation

Synthesis of metalloporphyrin monomer. Zn(II) 5,10,15,20-Tetrakis(4-bromophenyl) porphyrin (ZnBPP) was obtained by heating BPP (496.9 mg, 0.50 mmol), zinc acetate dihydrate (219.5 g, 1.00 mmol) in CHCl<sub>3</sub> solution at 140 °C for 12 h under N<sub>2</sub> atmosphere. After evaporation of the solvent, the product was washed with deionized water and further purified by column chromatography to obtain the purple ZnBPP powder; TOF-MS ( $m/z$ ) calcd. for C<sub>44</sub>H<sub>24</sub>Br<sub>4</sub>N<sub>4</sub>Zn [M + 1]<sup>+</sup> 993.70, found 993.63. Similarly, Cu(II) 5,15-bis(pentafluorophenyl)-10,20-bis(4-ethynylphenyl) porphyrin (CuFPP) are prepared by using FPP and copper acetate dihydrate precursors; TOF-MS ( $m/z$ ) calcd. for C<sub>48</sub>H<sub>18</sub>F<sub>10</sub>N<sub>4</sub>Cu [M + 1]<sup>+</sup> 903.07, found 903.04.

Synthesis of ZnCu-COF. The ethynyl-linked ZnCu-COF was prepared by polymerizing ZnBPP and CuFPP monomers (Scheme S1). Briefly, a Pyrex tube was added with ZnBPP (9.9 mg, 0.01 mmol), CuFPP (27.1 mg, 0.03 mmol), triethylamine (2.0 mL) and tetrahydrofuran (6.0 mL). After fully stirring, the triphenylphosphine (2.6 mg), Pd (II) acetate (6.7 mg) and cuprous iodide (1.9 mg) were charged into Pyrex tube for polyreaction. Degassed by three freeze-pump-thaw cycles and then sealed under vacuum, the tube was heated with 130 °C for 120-h at oven. The resulting precipitate was collected by centrifugation, and exhaustively washed by Soxhlet extractions with tetrahydrofuran and chloroform for 72-h. Finally, the brown-black ZnCu-COF was dried under vacuum oven at 80 °C, with yield of 82.7% on basis of ZnBPP monomer. Zinc and Copper element was analyzed as 3.06 wt% and 5.93 wt%, respectively, using inductively coupled plasma-optical emission spectrometry (ICP-OES). For comparison, Zn-COF and Cu-COF counterparts were prepared via the similar procedure by using the corresponding non-metallic porphyrin monomers.

### 2.2. Material characterization

Bruker miniflex600 powder X-ray diffractometer (PXRD) using Cu



**Scheme 1.** Illustration of self-built dinuclear-site photogate that results in fast kinetics for CO<sub>2</sub> photoreduction to HCOOH.

K $\alpha$  radiation ( $\lambda = 0.154$  nm) was used to analyze the crystal phase composition of products. XPS measurement was performed using Al K $\alpha$  radiation with an energy of 15 kV/150 W. High-angle annular dark-field or bright-field scanning transmission electron microscopy (HAADF or BF-STEM) characterization and corresponding energy-dispersive spectroscopy (EDS) were conducted on holey Au grids at a JEOL JEM-ARF200F TEM/STEM system with a spherical aberration corrector operated at 200 kV with a Schottky cold-field emission gun. Diffuse reflectance spectra (DRS) were recorded on UV1800 SHIMADZU. Raman spectra were obtained from Horiba Jovin Yvon equipped with Nd:Yag laser (785 nm). The Zinc and/or Copper contents were determined by inductively coupled plasma atomic emission spectroscopy (ICP-AES) analysis with an IRIS Intrepid II XRP instrument. CO<sub>2</sub> adsorption experiments were carried out at 298 K using a gas adsorption analyzer (Beijing JWGB Sci & Tech Co., Ltd).

Static and time-resolved X-ray absorption spectroscopies. X-ray absorption spectroscopy (XAS) data was measured in Nano-crystallography and Coherence Imaging experimental station with the BL01C1 beamline facility. The electron storage ring was maintained at 3.0 GeV along with changeable beam current. The monochromatic beam was provided by a double crystal Si (111) monochromator, which was equipped with second crystal for detuning monochromatic beam to reduce the high harmonic components in the X-ray beam. Data collection was performed at room temperature in the fluorescence mode by using Ge detector.

Zn/Cu K-edge X-ray absorption spectroscopy, including X-ray absorption near-edge structure (XANES) and extended X-ray absorption fine structure (EXAFS), was measured to provide coordination information on its local electronic and geometric structure. The raw data were dealt with IFEFFIT software package, following a calibrated, background subtracted, and normalized process in Athena software. Fourier-transform was performed on the k<sup>2</sup>-weighted EXAFS oscillations. The amplitude reduction factor S<sub>0</sub><sup>2</sup> for Zn and Cu K-edge was determined by fitting the reference Zn foil and Cu foil, which was fixed at 0.82 and 0.80 by fixing N as their known crystallographic values, respectively. As seen from Table S4, structural parameters, such as coordination numbers (N), bond length (R), the Debye-Waller factor ( $\sigma^2$ ), inner potential shift ( $\Delta E_0$ ) and goodness of fit (R factor) were obtained from the fitting result.

The pump-probe time-resolved X-ray absorption experiment (TR-XAS) was measured at Zn/Cu K-edge with an X-ray spot size of  $25 \times 15 \mu\text{m}^2$  at the sample position. The photocatalyst was dispersed in CH<sub>3</sub>CN/H<sub>2</sub>O solvent, containing the same ingredient and concentration as CO<sub>2</sub> photoreduction experiment. To circumvent sample damage from high-energy laser and X-ray pulse, the dispersion liquid was circulated via sample jet system, which consists of peristaltic pump (Masterflex), sample reservoir, stainless steel tube and its support. The sample was pumped from the reservoir by a peristaltic pump to the stainless-steel tube, forming a 150- $\mu\text{m}$  thickness liquid jet with  $\sim 1$  mL/s flow rate inside an CO<sub>2</sub>-purging jet chamber. The solution refluxed to the reservoir and was continuously circulated. Especially, the dispersion liquid reservoir was bubbled with ultrapure CO<sub>2</sub> to hold a saturated CO<sub>2</sub> atmosphere on whole experiment. Data was recorded at a rate of 60 Hz. The 400-nm excitation pulses, impinging on the sample at a rate of 30 Hz, had 3.7  $\mu\text{J}$  energy and were produced by second harmonic generation of 800-nm pulses with a pulse duration of 110 fs FWHM from an amplified Ti:Sapphire laser system. The excitation focus was  $65 \times 65 \mu\text{m}^2$  FWHM at the sample position.

In-situ diffuse reflectance infrared Fourier transform spectra. In-situ diffuse reflectance infrared Fourier transform spectra (DRIFTS) of CO<sub>2</sub>/H<sub>2</sub>O on these COFs sample under light irradiation was measured on Thermo Electron Nicolet iS50 spectrometer, equipped with liquid N<sub>2</sub> cooled HgCdTe (MCT/A) detector and  $2 \text{ cm}^{-1}$  resolution by using 64 scans. 2-mL suspension catalyst, containing the same ingredient and concentration of CO<sub>2</sub> photoreduction experiment in CH<sub>3</sub>CN/H<sub>2</sub>O solvent, was dispersed on the DRIFTS accessory, and then vacuum

treatment at 120 °C for 1-h was necessary to remove air impurities. Subsequently, humid CO<sub>2</sub> gas was purged into the reactor until 1 atm. Once the adsorption of CO<sub>2</sub>/H<sub>2</sub>O reaches equilibrium, the background is deducted, and then 150-W Xe-lamp was used to illuminate the sample through a quartz window to record IR signals at different time intervals. IR spectrum was collected when it was further stabilized.

Photoelectrochemical measurements. Electrochemical impedance spectra was obtained at standard three-electrode system using CHI Model 617B electrochemical analyzer, where Pt wire and Ag/AgCl were the counter electrode and reference electrodes, respectively. The working electrode was prepared by spinning photocatalyst suspension containing nafion solution (200  $\mu\text{L}$ ,  $0.02 \text{ mg mL}^{-1}$ ) onto In-doped SnO<sub>2</sub>-coated glass, which was placed in oven at 100 °C for 3 h to dry the solvent and solidify the samples. In a typical run, the three electrodes were immersed into a suspension containing Na<sub>2</sub>SO<sub>4</sub> solution (1.0 M) during on-off period of the 150 W Xe-lamp solar simulator equipped with AM 1.5 G filter.

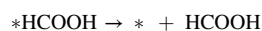
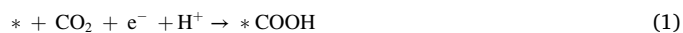
### 2.3. Computational details

In the DFT calculations, only a portion of the porphyrin ring was drawn to exhibit the configuration of the active center, but the whole COF cell were chosen as the model. Theoretical calculations were performed at the Perdew-Burke-Ernzerhof (PBE) exchange functional level. Vertex positions were obtained from Reticular Chemistry Structure Resource. The staggered arrangement for the COFs was also examined by offsetting the alternating stacked units from the eclipsed model.

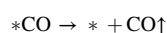
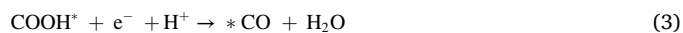
The unit cell structures of the eclipsed AA and staggered AB stacking modes were optimized using the density-functional tight-binding (DFTB) method, which is an approximate density functional theory method based on the tight binding approach and utilizes an optimized minimal Slater-type all-valence basis set in combination with a two-center approximation for Hamiltonian matrix elements. The Coulombic interaction between partial atomic charges was determined by using the self-consistent charge formalism. Dispersion correction was employed in all calculations to describe van der Waals and  $\pi$ -stacking interactions.

Pawley refinement was carried out by using Reflex package. Unit cell dimension was set to the theoretical parameters. The Pawley refinement was performed to optimize the lattice parameters iteratively until the  $R_{wp}$  value converges and the observed overlay with refined profiles shows good agreement. The pseudo-Voigt profile function was used for whole profile fitting, and Berrar-Baldinozzi function was used for asymmetry correction during the refinement processes. Line broadening from crystallite size and lattice strain were both considered. The lattice constants (Table S2–3) for ZnCu-COF with AB-eclipsed model was optimized with orthorhombic unit cell ( $a = b = 43.7238 \text{ \AA}$ ,  $c = 3.313 \text{ \AA}$ ;  $\alpha = \beta = \gamma = 90^\circ$ ) with C222 (D2–6) space group. According to the optimized crystal structures, band structure, orbitals, density of states, and electrostatics were performed using the same method and setup as the crystal optimization.

Moreover, based on the DRIFTS analysis, the possible reduction path for these COFs catalytic system could be as follows, where the asterisks denote active sites and the vertical arrows represent the produced gas in the intermediate reaction.



or





Gibbs free energies of each intermediate were calculated at 298.15 K from  $G = E_{\text{DFT}} + E_{\text{ZPE}} - TS$ , where  $E_{\text{DFT}}$  is the electronic energy calculated with DMol3,  $E_{\text{ZPE}}$  is the zero-point energy and TS is the entropy contribution. Standard ideal gas methods were employed to compute  $E_{\text{ZPE}}$  and TS from temperature, pressure and the calculated vibrational

energies. Particularly,  $G[e^- + \text{H}^+] = 1/2 G[\text{H}_2] - eU$ ,  $U$  is the applied overpotential,  $e$  is the elementary charge, and here  $U = 0$  V versus reversible hydrogen electrode. The free energy changes ( $\Delta G$ ) relative to an initial state can be obtained by the difference between products and reactants at every step.

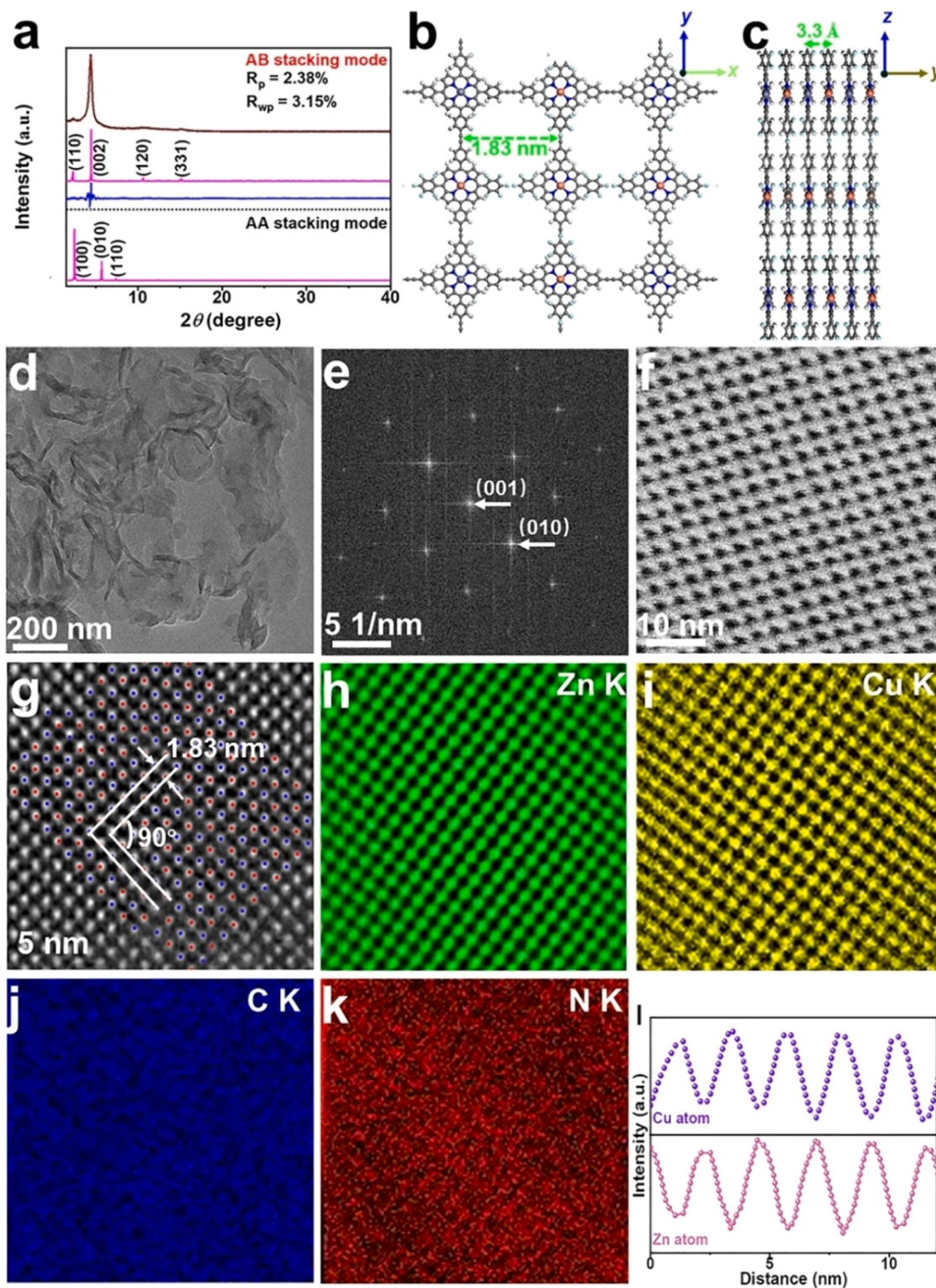


**Fig. 1.** Structural analyses of ZnCu-COF. (a) Typical PXRD patterns of ZnCu-COF with AA-/AB-stacked modes (experimental profiles in black, Pawley-refined profiles in red, predicted profiles in magenta, and differences in blue). (b,c) Topology of ZnCu-COF with AB stacking mode viewed along the z- and x-axes. (d) High-resolution AC-TEM, (e) SAED pattern, filtered, (f) AC-BF-STEM, (g) AC-ADF-STEM, (h–k) corresponding atom mappings, and (l) relative Zn/Cu-atom spatial location in ZnCu-COF.



## 2.4. Isotope labeling measurement

The isotope labeling measurement was carried out by using  $^{13}\text{CO}_2$  gas (isotope purity, 99%) instead of pure  $^{12}\text{CO}_2$  gas (Chemical purity, 99.999%) as the carbon source with the same photocatalytic process. The photocatalytic gas species was separated by gas spectrometry columns into individual substances. As the separated substances emerge from column, they flow into electron ionization equipment to ionize and fragment analyte molecules. The separated gas products were analyzed by mass spectrometry (JMS-K9, JEOL-GCQMS, USA) equipped with different kinds of column for detecting the products of  $^{13}\text{CO}$  (HP-MOLESIEVE, USA) and source of  $^{13}\text{CO}_2$  (HP-PLOT/Q USA), respectively. In addition, the liquid product from the photoreaction of ZnCu-COF with  $^{13}\text{CO}_2$  was detected by the  $^{13}\text{C}$  NMR spectra.

## 2.5. Photocatalytic $\text{CO}_2$ reduction test

The  $\text{CO}_2$  photoreduction experiment was performed in an enclosed glass reactor with total volume of 230 mL under a 150 W Xe-lamp (Abet Technologies) irradiation equipped with an AM 1.5 G filter. The distance from the lamp to the sample was about 12 cm, the intensity of Xe-lamp light was calibrated to be  $100 \text{ mW cm}^{-2}$  to the quartz reactor surface (calibrated by an CEL-NP2000 Optical Power Meter), and the irradiation area was  $5.65 \text{ cm}^2$ . In a typical test, catalysts (15 mg) were dispersed in 15 mL of solution (10 mL acetonitrile, 2 mL deionized water, and 3 mL triethanolamine). The reactor was vacuumed and purged with high purity  $\text{CO}_2$  for 30 min, respectively, which was repeated two times. During the irradiation, the gas products were analyzed by gas chromatograph (Agilent 8890, TDX-01 column,  $5 \text{ \AA}$

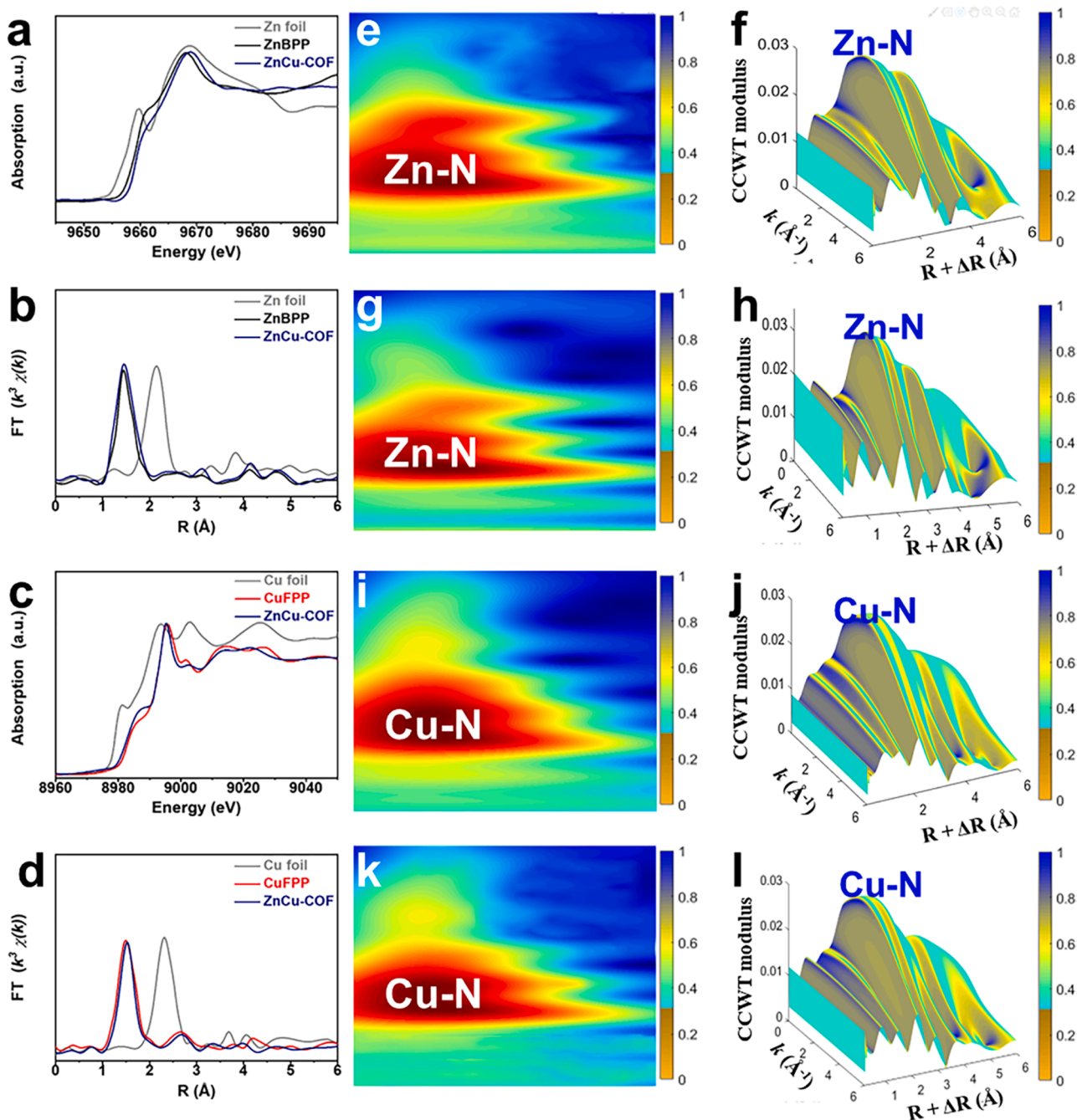


**Fig. 2.** X-ray absorption spectroscopic analyses. (a,b) Normalized XANES, (c,d) EXAFS, and (e–l) Cauchy wavelet transform (e, f ZnBPP monomer and g, h ZnCu-COF at Zn K-edge and i, j CuFPP monomer and k, l ZnCu-COF at Cu K-edge).

molecular sieve column) equipped with a flame ionized detector (FID) and thermal conductivity detector (TCD), which 0.5 mL of gas was taken out from the reactor at regular intervals. The liquid products were analyzed by high performance liquid chromatography and  $^{13}\text{C}$  NMR spectroscopy. For the cyclic test, the used sample was centrifuged from the reaction solution and re-dispersed in the fresh solution for the next cycle of activity test. In the present photoreaction systems, hydrogen ( $\text{H}_2$ ), carbon monoxide ( $\text{CO}$ ) and formic acid ( $\text{HCOOH}$ ) are the main products, and no other product such as  $\text{CH}_3\text{OH}$ ,  $\text{C}_2\text{H}_4$  and  $\text{C}_2\text{H}_6$  (using GC-FID detector) was detected. Furthermore, control experiments exhibited no reduced product detected from the photoreaction system without photocatalyst, light irradiation or  $\text{CO}_2$  gas, which suggests that the reduced products ( $\text{CO}$ ,  $\text{HCOOH}$ ) of  $\text{CO}_2$  are originated from the photoreaction over the photocatalysts.

### 3. Results and discussion

#### 3.1. Crystal phase and microstructure analyses

The ZnCu-COFs were developed by coupling Zn(II) 5,10,15,20-Tetrakis(4-bromophenyl) porphyrin (ZnBPP, Figs. S1,2) and Cu(II) 5,15-bis(pentafluorophenyl)-10,20-bis(4-ethynylphenyl) porphyrin (CuFPP, Figs. S3,4) [39,40]. The Zn and Cu content was found to be 3.06 and 5.93 wt% (Table S1). For comparison, the Zn-COF and Cu-COF

counterparts were prepared through a similar procedure by using the corresponding non-metallic porphyrin monomers. The ZnCu-COF exhibited Fourier transform infrared (FTIR) peaks, similar to ZnBPP and CuFPP monomers, but the vibration peaks for C-Br ( $\sim 727\text{ cm}^{-1}$ ) and  $\text{C}\equiv\text{C}$  ( $\sim 2783\text{--}3006\text{ cm}^{-1}$ ) weakened after the polymerization (Fig. S5) [39–41]. Further, the ZnCu-COF displayed alkynyl-group stretching vibration Raman peaks (Fig. S6) and solid-state  $^{13}\text{C}$  nuclear magnetic resonance (NMR) bands (Fig. S7) [25–29]. These chemical structure analyses suggest the successful formation of the porphyrin-based COF.

Powder X-ray diffraction (PXRD) analysis of the ZnCu-COF was performed, and four main diffraction peaks at  $2.23^\circ$ ,  $4.42^\circ$ ,  $10.59^\circ$ , and  $15.17^\circ$  (Fig. 1a), corresponding to (110), (002), (120) and (331) crystal facets, respectively, were observed [42]. The crystal model was optimized by density-functional tight-binding calculations. Obviously, the calculated diffraction patterns of the AB-eclipsed stacking model matched well with the experimental PXRD patterns, suggesting that the ZnCu-COF adopted an AB-stacked layered structure (Table S2–3). Furthermore, the Pawley refinement data were in good agreement with the experimentally observed data as evidenced by the negligible difference between the two data. This indicates that the refined ZnCu-COF topology exhibit a planar structure with theoretical pore size and  $d$ -spacing of 1.83 and 0.33 nm, respectively (Fig. 1b,c and Fig. S8,9). The detailed crystal structure information, including the unit cell parameters, are available found in Supplementary information. Further,

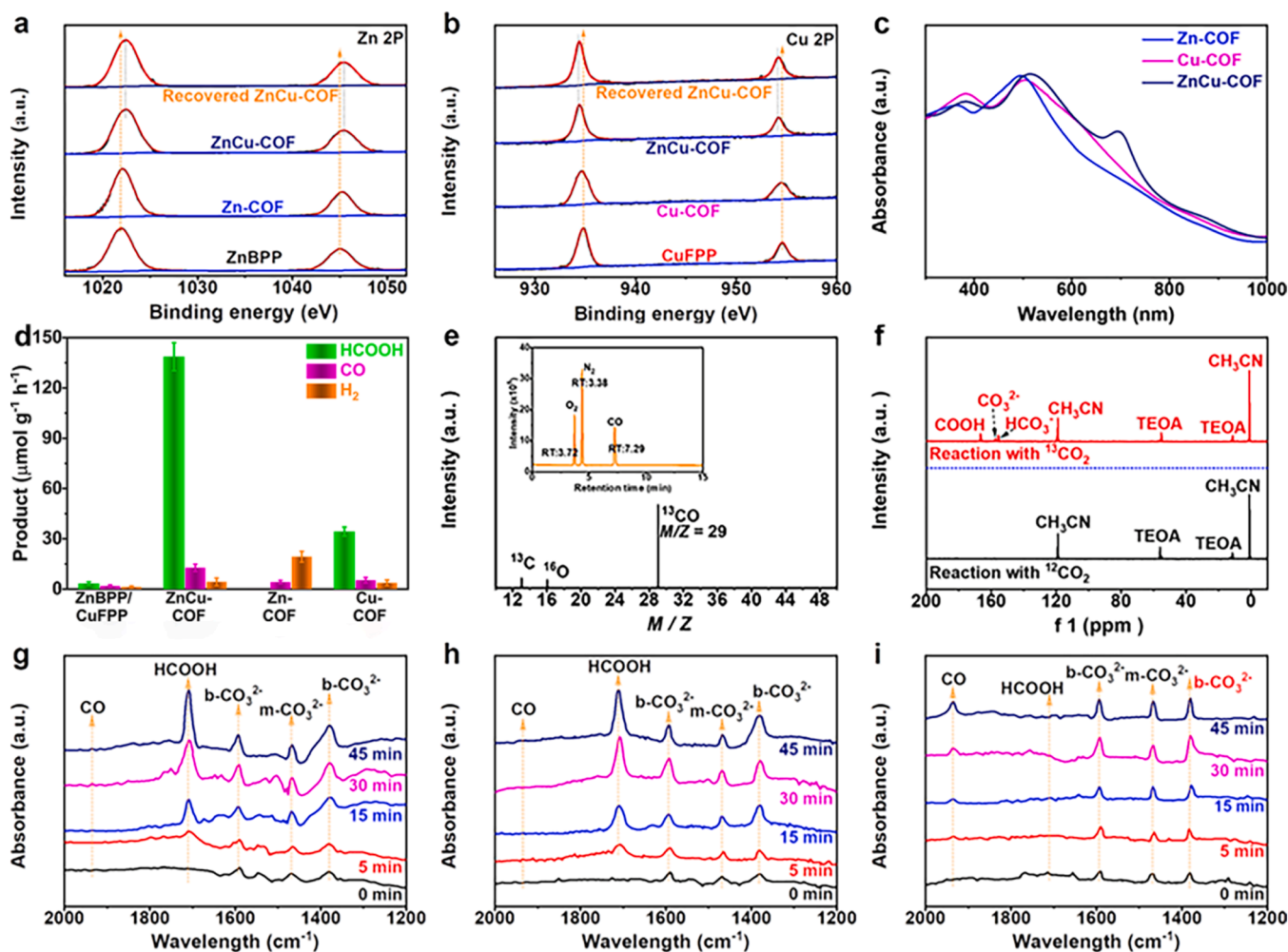


**Fig. 3.** Photocatalytic  $\text{CO}_2$  assessments and intermediates identifications. High-resolution (a) Zn 2p and (b) Cu 2p XPS spectra of the precursors and COFs as well as the recovered ZnCu-COF after 24-h photoreaction. (c) DRS spectra of the COFs. (d) Production rates of  $\text{HCOOH}$ ,  $\text{CO}$ , and  $\text{H}_2$  over Zn-COF, Cu-COF, and ZnCu-COF. (e)  $^{13}\text{C}$  mass spectrum of the gaseous product with total ion chromatogram (inset) and (f)  $^{13}\text{C}$  NMR spectra of the liquid product of ZnCu-COF. In-situ DRIFTS of (g) ZnCu-COF, (h) Cu-COF, and (i) Zn-COF.

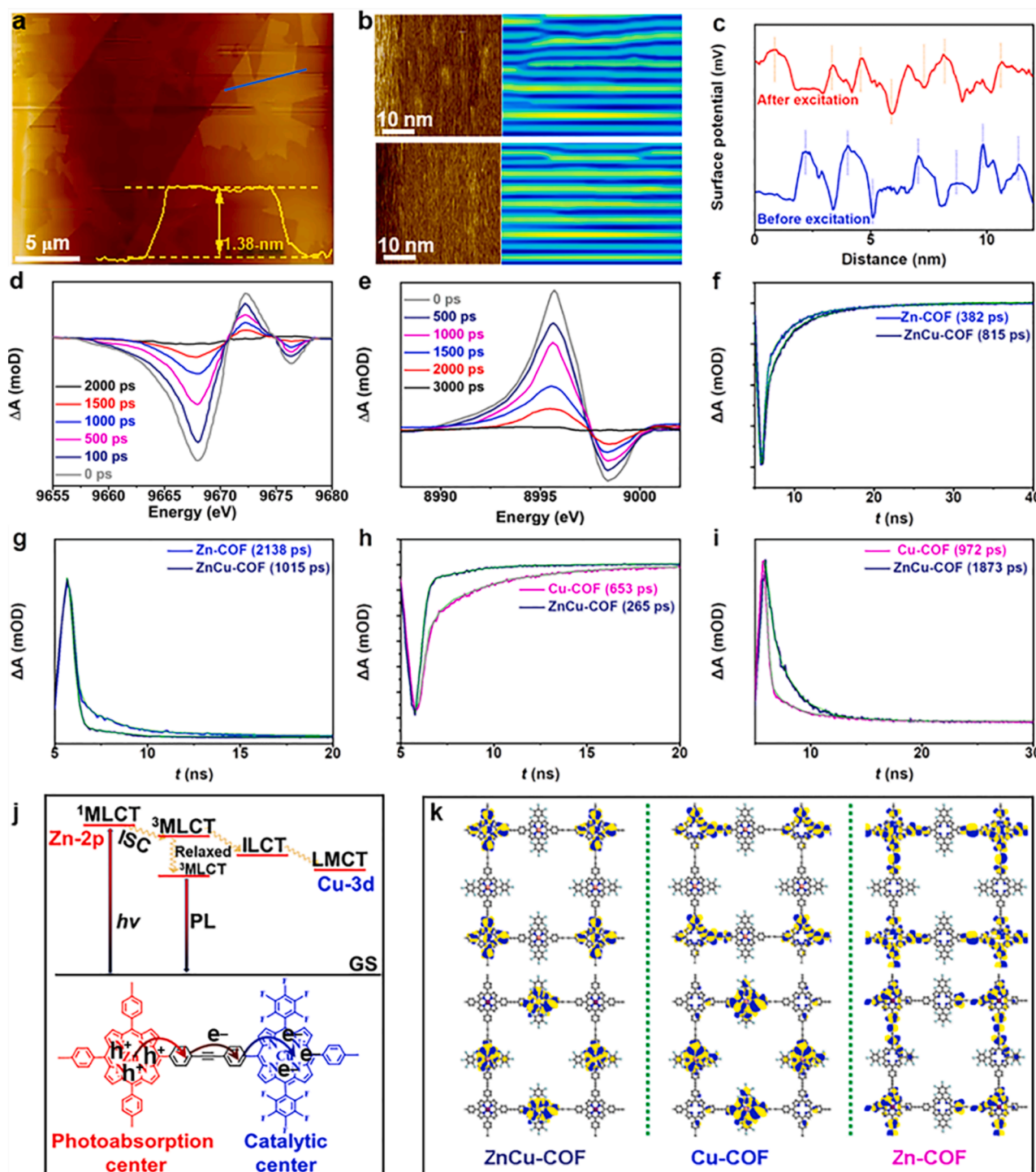


**Fig. 4.** Information on the excited state dynamics of ZnCu-COF. (a) AFM image, (b) KPFM surface potential distribution and its color-coded contour map before (bottom) and after (top) 400-nm pulse excitation, (c) surface potential line scan, and TR-XAS at (d) Zn and (e) Cu K-edges of ZnCu-COF. Kinetic analysis of excited  $^*Zn(II)$  signals (f) growth and (g) decay at 9667.3 and 9676.5 eV, and the excited Cu signals (h) growth and (i) decay at 8995.6 and 8998.4 eV. (j) Simplified model for electron diffusion within ZnCu-COF (ILCT = intra-ligand charge transfer, LMCT = ligand-to-metal charge transfer, GS = ground state, PL = photoluminescence, ISC = intersystem crossing). (k) Charge density distribution of ground-state (top) and excited-state (bottom) in Zn-, Cu-, and ZnCu-COFs.

the porosity of the porphyrin COFs was characterized by nitrogen sorption isotherms measured at 77 K (Fig. S10–12). The COFs exhibited typical type-IV sorption isotherm curves with microporous characterization. The Brunauer–Emmett–Teller (BET) surface areas were calculated as 973 (Zn-COF), 968 (Cu-COF), and 981 (ZnCu-COF)  $m^2 g^{-1}$ , respectively. All these COFs mainly showed pore size distributions around  $\sim 1.85$  nm according to the Horvath–Kawazoe model, matching

well with the calculated pore sizes in the AB-eclipsed stacking geometry. Furthermore, thermogravimetric analysis (Fig. S13–15) showed that these three COFs were thermo-stability up to 360  $^{\circ}C$ . The chemical-stable crystallinity of ZnCu-COF was explored by dispersing it into different solvents (*n*-hexane, 0.1 M HCl, 6 M NaOH). Notably, when comparing with the raw sample, the immersed ZnCu-COF exhibited intense PXRD patterns (Fig. S16a) without significant change in the peak



position and intensity. As contrasted to the original spectra (Fig. S5), the FTIR (Fig. S16b) of ZnCu-COF showed typical vibrations of pyrrole and benzene rings ( $\sim 752\text{--}1038\text{ cm}^{-1}$ ) [39] and  $\text{--C}\equiv\text{C--}$  ( $\sim 2783\text{--}3006\text{ cm}^{-1}$ ) [37], and the strong characteristic metal–N (Zn–N, Cu–N) peaks of ZnCu-COF could be observed at  $1071\text{ cm}^{-1}$  [40]. In addition, the detection results of ICP-OES confirmed that there was no Zn/Cu element signal in the treatment supernatant, which was centrifugally separated from the ZnCu-COF suspension after treated with these different solutions for 24-h. These results indicate that the high crystallinity is retained under harsh conditions.

To gain more insights into the ZnCu-COF microstructures, scanning electron microscopy (SEM) and transmission electron microscopy (TEM) were also performed. It can be seen that the SEM and TEM images exhibit NS structures with transparent appearance and micrometer lateral dimension (Fig. 1d and Fig. S17). The sharp selected area electron diffraction (SAED) pattern of the ZnCu-COF clearly revealed visible bright spots with a tetragonal pattern due to the orderly stacked structure (Fig. 1e), and the orthogonal lattice unveiled its orthorhombic crystal system. Most impressively, more detailed structural information for the ZnCu-COF NSs was further visualized by using aberration-corrected bright-field scanning transmission electron microscopy (AC-BF-STEM, Fig. 1f). A periodic square pore skeleton with well-defined building units was clearly observed because of the ultrathin structure and high crystallinity, and the observed bright square spots and black contrasts corresponded to the metalloporphyrin compartments and one-dimension pore channels, respectively. Moreover, as shown in the aberration-corrected annular dark-field scanning transmission electron microscopy (AC-ADF-STEM, Fig. 1g) images, the Zn (red dots) and Cu (blue dots) single atoms exhibited a cross-distribution matrix on the ZnCu-COF NSs uniformly [11,42], and the measured distances were  $a = b = 1.83 \pm 0.2\text{ nm}$ ,  $\alpha = 90 \pm 0.3^\circ$ , matching well with those of the simulated structure and further confirming the successful fabrication of the ZnCu-COF NSs. The corresponding energy-dispersive X-ray (EDX) elemental mappings for ZnCu-COF (Fig. S18, Fig. 1h–k) confirmed that the Zn, Cu, C and N atoms were atomically cross dispersed on the skeletons, presenting a  $90^\circ$  phase difference of the Zn/Cu-atom spatial location (Fig. 1l).

X-ray absorption near edge structure (XANES) calculations were performed to further explore the local coordination environment and electronic structure of the Zn/Cu atoms on the ZnCu-COF. According to the Zn and Cu foil reference samples, whose first neighbor shells were fitted with Zn–Zn and Cu–Cu backscattering coordination, respectively, the  $k^3$ -weighted X-ray absorption fine structure (EXAFS) oscillations of the Zn K-edge and Cu K-edge, as well as their Fourier transformed radial distribution functions could be obtained. The Zn K-edge absorption-starting position of the ZnCu-COF showed a positive shift due to a decreased electron density, compared to the ZnBPP precursors (Fig. 2a), whereas the Cu K-edge absorption-starting energy exhibited a negative shift because of the electronic configuration, compared to the CuFPP precursors (Fig. 2b). This implies that the exciton energy transferred from the ZnBPP to CuFPP units in the ZnCu-COF heterostructure [14, 43]. The  $R$ -space Fourier transformation of the Zn K-edge EXAFS spectrum of the ZnCu-COF displayed a main peak at  $1.76\text{ \AA}$  (Fig. 2c, Supplementary Table 4), corresponding to the Zn–N first shell, while no additional Zn–Zn atomic scattering as Zn foil (at  $2.43\text{-}\text{\AA}$ ) was detected. Similarly, the Cu K-edge  $R$ -space Fourier transformation of the ZnCu-COF EXAFS spectrum exhibited a peak at  $1.71\text{ \AA}$ , corresponding to the Cu–N shell scatterer, and no additional Cu–Cu interaction as Cu foil (at  $2.61\text{ \AA}$ ) was observed (Fig. 2d). The fitted EXAFS spectrum showed that the Zn and Cu coordination number in the precursors and ZnCu-COFs was determined as  $\sim 4$  for the existing metalloporphyrin structures (Fig. S20 and Table S4). This clearly indicates single-atom distribution of Zn/Cu in the ZnCu-COFs rather than metal clusters, as further conjectured by the continuous Cauchy wavelet transformation (Fig. 2e–l and Fig. S20).

The survey spectra (Fig. S21), obtained via X-ray photoelectron

spectroscopy (XPS), indicate that Zn, Cu, C, N, F, and Br coexisted in the precursors and COFs. The high-resolution Zn 2p XPS spectra (Fig. 3a) showed that ZnBPP had  $\text{Zn}^{\text{II}} 2p_{3/2}/2p_{1/2}$  binding energy (BE) peaks of  $1021.88/1044.91$  [44], which showed a positive shift for Zn-COF ( $\sim 0.25\text{ eV}$ ) and ZnCu-COF ( $\sim 0.43\text{ eV}$ ), ascribable to a decreased electron density of the ZnBPP cores. Similarly, a negative shift for the  $\text{Cu}^{\text{II}} 2p_{3/2}/2p_{1/2}$  spectrum (Fig. 3b) could be observed for Cu-COF ( $\sim 0.28\text{ eV}$ ) and ZnCu-COF ( $\sim 0.55\text{ eV}$ ), compared to the CuFPP precursor ( $934.88/954.67$ ), because of an increased electron density around the CuFPP cores [45].

As evident from the ultraviolet-visible (UV-Vis) diffuse reflection spectra (DRS) shown in Fig. 3c, all the three COFs showed a strong intramolecular  $\pi\text{--}\pi^*$  transition ( $\sim 320\text{--}580\text{ nm}$ ). Compared to the solution absorption spectra of ZnBPP (BPP) and CuFPP (FPP) monomers (Fig. S1 and Fig. S3), the DRS spectra indicated that these COFs showed much unobvious B-band and Q-band absorptions derived from the increasing  $\pi$ -bond conjugated system, which exhibited excellently light absorption ability in the range of  $300\text{--}1000\text{ nm}$ . Particularly, when comparing with the Zn-COF and Cu-COF, the ZnCu-COF exhibited a broadband absorption feature with distinct absorption peak at  $\sim 687\text{--}773\text{ nm}$  in the visible light region, which can be ascribable to the intensive metal-to-metal charge transfer behaviors from ZnBPP to CuFBB cores [46,47], further demonstrating that energy transfer and electron diffusion occurred among the heterobimetallic porphyrin cores in the extended two-dimensional networks of ZnCu-COF. Further, the optical bandgap energies ( $E_g$ ) were  $1.85$  (Zn-COF),  $1.74$  (Cu-COF), and  $1.78$  (ZnCu-COF) eV, as evaluated using the Kubelka–Munk method (Fig. S22–24) [6,8,48]. Additionally, their valence band (VB, vs. NHE) potentials were  $1.26$  (Zn-COF),  $1.06$  (Cu-COF), and  $0.95$  (ZnCu-COF) eV, which were measured via UV photoelectron spectroscopy performed in an ultrahigh vacuum chamber (Fig. S25–27). Therefore, the relative energy band structures of these COFs (Fig. S28) unveiled that all the conductive band (CB) potentials were more negative than those of some typical photocatalytic products, such as  $\text{H}_2$  ( $0\text{ eV}$ ),  $\text{HCOOH}$  ( $-0.61\text{ eV}$ ), and  $\text{CO}$  ( $-0.53\text{ eV}$ ) with reference to NHE [25,49], theoretically available for photocatalytic  $\text{H}_2$  production, and  $\text{CO}_2$  reduction.

### 3.2. Activity analyses for $\text{CO}_2$ photoreduction

Photocatalytic  $\text{CO}_2$  reduction over these heterobimetallic COFs was conducted on  $\text{CH}_3\text{CN}/\text{H}_2\text{O}$  ( $\text{CO}_2$  solubility solvent) and triethanolamine (TEOA, sacrificial electron donor) under a  $150\text{-W}$  Xe-lamp illumination (Fig. S29). As depicted in Fig. 3d, the Zn-COF merely formed  $\text{CO}$  ( $4.2\text{ }\mu\text{mol g}^{-1}\text{ h}^{-1}$ ) and  $\text{H}_2$  ( $19.3\text{ }\mu\text{mol g}^{-1}\text{ h}^{-1}$ ), but the Cu-COF delivered a significant yield of  $\text{HCOOH}$  ( $34.3\text{ }\mu\text{mol g}^{-1}\text{ h}^{-1}$ ), compared to  $\text{CO}$  ( $5.3\text{ }\mu\text{mol g}^{-1}\text{ h}^{-1}$ ) and  $\text{H}_2$  ( $3.7\text{ }\mu\text{mol g}^{-1}\text{ h}^{-1}$ ), suggesting that the type and position of the chelated metal ions in the COFs can greatly affect the production of species during the  $\text{CO}_2$  reduction. Furthermore, the physical mixture of the ZnBPP/CuFPP precursors (molar ratio of  $1:2$ ) exhibited a negligible photoactivity of  $\text{HCOOH}/\text{CO}/\text{H}_2$  ( $3.3/1.8/1.2\text{ }\mu\text{mol g}^{-1}\text{ h}^{-1}$ ), but the ZnCu-COF showed an excellent production rate of  $\text{HCOOH}$  ( $138.6\text{ }\mu\text{mol g}^{-1}\text{ h}^{-1}$ ),  $\text{CO}$  ( $12.7\text{ }\mu\text{mol g}^{-1}\text{ h}^{-1}$ ), and  $\text{H}_2$  ( $4.3\text{ }\mu\text{mol g}^{-1}\text{ h}^{-1}$ ) with  $89.1\%$   $\text{HCOOH}$ -evolving selectivity. These results demonstrate that both the heterobimetallic centers and conjugated framework are important for efficient  $\text{CO}_2\text{RR}$ . The most likely reason is that the formation of photoexcited electron transfer channels and increased electron delocalization degree within the COF NSs promote charge separation, and thus, more active electrons can be used for the  $\text{CO}_2\text{RR}$ .

Additional control experiments revealed that no products could be detected without the photocatalyst,  $\text{CO}_2$ , or light irradiation. To further confirm the carbon source of the  $\text{HCOOH}$  and  $\text{CO}$  products, the  $^{13}\text{C}$  isotope trace experiment was employed in the reaction. The mass spectrum only exhibited the  $^{13}\text{C}$  signal peaks at  $m/z = 29$  (Fig. 3e and Fig. S30), and the  $^{13}\text{C}$  NMR spectrum showed the  $\text{HCOOH}$  signal with a peak at  $166.36\text{ ppm}$  (Fig. 3f), unambiguously verifying that the carbon

source of HCOOH and CO products indeed comes from the CO<sub>2</sub> photo-reduction. The catalyst photostability of ZnCu-COF was further evaluated through recycling experiments (Fig. S31–S33), and the photoactivity could be retained during three consecutive runs for a total 24-h irradiation. Moreover, the recovered ZnCu-COF photocatalyst after the three consecutive photoreaction cycles exhibited a DRS (Fig. S34a) and PXRD (Fig. S34b) profiles very similar to that of the original one. Also, the survey XPS (Fig. S21) spectra of the recovered ZnCu-COF product after 24-h photocatalytic reaction indicates that Zn, Cu and F still coexist in the COFs' skeleton. The high-resolution recovered Zn2p XPS (Fig. 3a) spectra has Zn<sup>II</sup> 2p<sub>3/2</sub>/2p<sub>1/2</sub> binding energy peaks at 1022.31/1045.34 eV, and the recovered Cu<sup>II</sup> 2p<sub>3/2</sub>/2p<sub>1/2</sub> (Fig. 3b) binding energy can be observed in 934.33/954.12 eV, which were the same to that of ZnCu-COF without 24-h photoreaction. These results indicate that the crystal phase, element composition and valence states of the ZnCu-COF composite are unchanged during the long-term photoreaction process, and thus has very high structural stability and no significant crystallinity destruction for the recovered ZnCu-COF after a long-time CO<sub>2</sub> photoreaction.

### 3.3. Discussion of the mechanism of activity enhancement

To give an insight on the underlying HCOOH/CO selectivity mechanism, in-situ diffuse reflectance infrared Fourier-transform spectroscopy (DRIFTS) was employed to detect the generated intermediate species during the photoreaction process. As seen in the in-situ DRIFTS of these COFs (Fig. 3g–i), the peaks at 1367 and 1593 cm<sup>-1</sup> were attributed to the symmetric/asymmetric stretching of bidentate carbonate (b-CO<sub>3</sub><sup>2-</sup>) when CO<sub>2</sub> adsorption reached equilibrium on the reaction sites [14,50], while the characteristic infrared bands of 1464 cm<sup>-1</sup> could be attributed to the stretching vibration of monodentate carbonate (m-CO<sub>3</sub><sup>2-</sup>). In particular, both the Cu-COF and ZnCu-COF exhibited a gradually strengthened signal of \*COOH group at 1710 cm<sup>-1</sup> over the irradiation time from 5-min to 45-min in CO<sub>2</sub>-saturated atmosphere, which was a key intermediate for the conversion of CO<sub>2</sub> to HCOOH and other useful fuels [21,51]. Contrastingly, new peak at 1917 cm<sup>-1</sup>, presenting increasing intensities during the prolonged irradiation time, could be merely observed in Zn-COF photocatalytic process, indicating that abundant \*CO intermediates were generated on the Zn-COF surfaces merely [52,53]. These results indicate that the Cu-contained COFs can contribute to the CO<sub>2</sub>-to-HCOOH conversion preferentially, whereas CO production is primarily produced in Zn-COF surface, because of different charge separation and intermediates binding strength.

Spatial potential distribution within the ZnCu-COF was further revealed via photoirradiated Kelvin probe force microscopy (KPFM) investigation to reveal the intraskeletal charge transfer behavior between the ZnBPP and CuFPP cores. In a typically illustrative line scan across the ZnCu-COF surface (Fig. 4a–c and Fig. S35), surface potential of the uniform and ultrathin NS-like ZnCu-COF (1.38 nm) showed a clearly differentiated fluctuation before and after the pulse excitation as compared with the silicon substrate. This fluctuation can be attributed to the energy transfer and electron diffusion [54,55]. Furthermore, operando time-resolved X-ray absorption spectroscopy (TR-XAS) of the Zn and Cu K-edges also showed a transient charge-transfer behavior and changed metal-centered valence state during the mediating photocatalytic CO<sub>2</sub> reduction reaction under a series of time delays between laser and X-ray pulses [56]. After initiated by a 400-nm femtosecond pump pulses, two negative absorption bands of the excited-state \*Zn(II) appeared at 9667.3 eV and 9676.5 eV (Fig. 4d and Fig. S36a), which was ascribed to single metal-to-ligand charge transfer (<sup>1</sup>MLCT) and triplet metal-to-ligand charge transfer (<sup>3</sup>MLCT) of the excited-state \*Zn(II) [56–58], respectively, and a positive ground-state bleaching band was observed at 9672.4 eV for the excited \*Zn(II). Further, the absorption peaks for photoexcitation-evolved Cu(I) and quenched ground-state Cu(II) were located at 8995.6 and 8998.4 eV, respectively (Fig. 4e and

Fig. S36b). Contrastingly, the excited-state Zn K-edge of the ZnCu-COF showed a more accelerated quenching, in a time period of 2000 ps than that of Zn-COF (4200 ps), and the Cu K-edge of the ZnCu-COF showed much more sluggish quenching than that of Cu-COF (1600-ps), indicating that the photogenerated electrons could unequivocally spread from the Zn photosensitizer cores to the CuFPP catalyst sites. To further prove the dynamic process, kinetic analysis of the transient signal was conducted at the Zn K-edge and Cu K-edge on the fixed energies (Fig. 4f–i). The excited \*Zn(II) and Cu(I) growth lifetimes were fitted to 382 (Zn-COF) and 653 ps (Cu-COF), respectively, while the ZnCu-COF showed an increased \*Zn(II) lifetime (815 ps) and decreased Cu(I) lifetime (265 ps) due to the shift in the growth equilibrium between the two heterobimetallic centers. Concurrently, the excited-state \*Zn(II) decay (1015 ps) in the ZnCu-COF was faster than that of Zn-COF, and Cu(I) bleaching recovery in the ZnCu-COF was slower than that of Cu-COF (972 ps), indicating an efficient photoelectron transfer from the ZnBPP to the CuFPP cores. These results indicate that the diatomic ZnCu-COF exhibited better intraskeletal-charge transfer efficiency than those of the single-atom Zn-COF and Cu-COF.

To further elucidate the effect of Zn/Cu atom on the electronic band structure and contribution of each related orbital to the  $E_{CB}$  and  $E_{VB}$  of these COFs, the band structure and electrostatic potentials were calculated using the first-principle pseudopotential methods according to density functional theory (DFT, Fig. S37). The observed bandgap and work function ( $\phi$ ) of the ZnCu-COF and Cu-COF were much more narrowed than those of the Zn-COF, showing a good agreement with the experimentally determined values. Partial density of state (DOS, Fig. S38) showed that the VB top of the ZnCu-COF was primarily derived from the hybridized Zn 2p orbitals, while the CB bottom was mainly composed of the unoccupied Cu(II) 3d orbitals, indicating that the cooperated Cu(II) at the pentafluorophenyl-porphyrin center beneficially promoted the intraskeletal photogenerated electron transfer from Zn-2p of ZnBPP to Cu-3d of CuFPP. Namely, the energy transfer and electron diffusion process over the intraskeletal PMD-based atom-site ZnCu-COF can be presented as Fig. 4j, which can be supported by the charge density difference distribution of ground-state and excited-state in these COFs (Fig. 4k). As observed, ground-state electrons of these three COFs were mostly delocalized over the BPP/ZnBPP cores, but the excited-state charge density distribution for the Cu-COF and ZnCu-COF homogeneously enriched the CuFPP cores, compared to the Zn-COF dispersed around the maternity and alkyne. The more accessible charge transfer between the Zn and Cu matrices resulted in a lowest charge transfer resistance ( $R_{ct}$ ) of electrochemical impedance spectroscopy (Fig. S39a) and highest photocurrent density (Fig. S39b) of ZnCu-COF in comparison to the Zn-COF and Cu-COF. These visualizations further verify that the Cu centers located in the matrix-bridging CuFPP can energetically accommodate the photoexcited electrons from the BPP or ZnBPP cores, and consequently act as single-atom active sites for CO<sub>2</sub> photoreduction.

Given that the activity and selectivity of CO<sub>2</sub>RR were related to CO<sub>2</sub> absorption and activation, DFT calculations between Zn (or Cu) site and CO<sub>2</sub> molecular were derived to decode how the Zn/Cu site affected the CO<sub>2</sub>RR photoactivity and selectivity (Fig. S40). The calculated CO<sub>2</sub> adsorption Gibbs free energy ( $\Delta G_{CO_2}$ ) at the Zn site of ZnBPP core in ZnCu-COF was 1.86 eV with a Zn–C length of 2.55 Å, whereas the Cu site of CuFPP core exhibited a higher  $\Delta G_{CO_2}$  (3.36 eV) and shorter Cu–C bond (1.98 Å), suggesting that the CO<sub>2</sub> molecules absorbed on the Cu site had much stronger interaction than that on Zn site, and this result was accorded with the CO<sub>2</sub> uptake experiment (Fig. S41), in which ZnCu-COF and Cu-COF showed the unexpectedly high CO<sub>2</sub> uptake capacities compared with that of the Zn-COF counterpart.

The projected DOS (PDOS) of Cu 3d orbitals in the ZnCu-COF and Cu-COF were analyzed before and after CO<sub>2</sub> absorption to reveal CO<sub>2</sub> activation. The Cu-3d DOS in the ground-state were mainly delocalized in the  $d_{yz}$ ,  $d_{zx}$ ,  $d_{z^2}$ , and  $d_{x^2-y^2}$  (Fig. 5a), and C-2p DOS of free CO<sub>2</sub>

molecular was in  $p_x$  and  $p_y$  (Fig. S42). Comparatively, on the excited-state Cu(I) site of ZnCu-COF and Cu-COF, Cu-3d DOS was less delocalized on the  $d_{yz}$ ,  $d_{xz}$ , and  $d_{x^2-y^2}$  orbitals (Fig. 5b) in comparison to their ground state, which was obviously localized to Cu-3d<sub>z<sup>2</sup></sub> orbital that passed through the Fermi level. Such redistribution of Cu-3d states at the excited Cu(I) site indicate the energy change of these orbitals. Possibly, after photoelectron transfer from the excited \*Zn(II) to the Cu site, the photogenerated electron caused Cu-3d<sub>z<sup>2</sup></sub> delocalization due to an increased orbital energy, which are beneficial to CO<sub>2</sub> activation along

with the Cu-3d<sub>z<sup>2</sup></sub> orbital coupling interactions. Moreover, as compared to the projected DOS of C atom in free CO<sub>2</sub> molecular (Fig. S42), 2p<sub>z</sub> state of C atom that absorbed on pyrrole N of FPP center on the excited Zn-COF was not variable apparently (Fig. 5c), but 2p<sub>z</sub> DOS of C atom (absorbed on the Cu site of excited ZnCu-COF and Cu-COF) showed an intensive increase. The alterations of C atom projected DOS in CO<sub>2</sub> molecular indicated that energy transfer and electron diffusion occurred from the excited Cu(I) site to CO<sub>2</sub> molecular orbital, mostly to 2p<sub>z</sub> orbital of C atom via (Cu-3d<sub>z<sup>2</sup></sub>)-(C-2p<sub>z</sub>) orbital coupling.

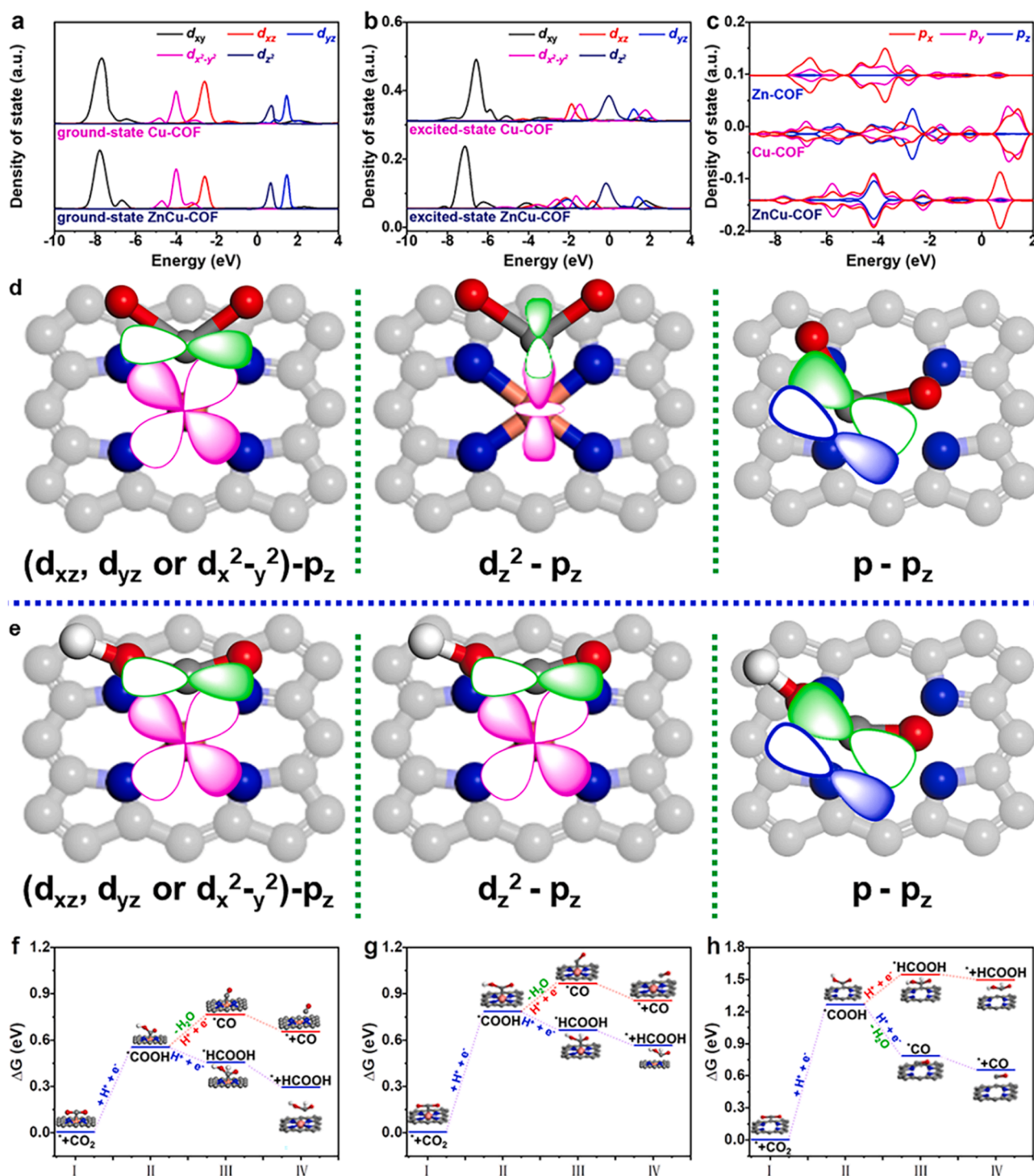


**Fig. 5.** Orbital coupling and free energy diagram of CO<sub>2</sub> photoreactions. 3d orbital projected DOS of Cu atom in the (a) ground-state and (b) excited-state COFs and (c) 2p orbital projected DOS of the excited C atom of CO<sub>2</sub> molecular (bonding with the excited Cu center of CuFPP or pyrrole N of FPP). Different coupling modes of (d) CO<sub>2</sub> and (e) \*COOH interacting with Cu-3d orbital or pyrrole N site. Free energy diagrams of CO<sub>2</sub>RR to HCOOH/CO on (f) ZnCu-COF, (g) Cu-COF, and (h) Zn-COF.



Based on overlap projected DOS (Fig. 5d,e and Fig. S43 and Table S5,6), we had evaluated different coupling strengths between Cu-3d atomic orbitals and C-2p<sub>z</sub> of adsorbed CO<sub>2</sub> or \*COOH intermediate in these COFs. From the integral area of orbital wave functions, the area was very low ( $8.71 \times 10^{-6}$ ) for the overlap orbital of pyrrole N and C-2p<sub>z</sub> of adsorbed CO<sub>2</sub> on FPP center of Zn-COF, but the (Cu-3d<sub>z<sup>2</sup></sub>)-(C-2p<sub>z</sub>) showed the strongest overlap ( $3.52 \times 10^{-2}$ ) than those of d<sub>xy</sub> ( $6.13 \times 10^{-4}$ ), d<sub>zx</sub> ( $7.35 \times 10^{-3}$ ), d<sub>yz</sub> ( $6.29 \times 10^{-3}$ ), and d<sub>x<sup>2</sup>-y<sup>2</sup></sub> ( $1.28 \times 10^{-3}$ ) orbital couplings in the CO<sub>2</sub>-adsorbed ZnCu-COF, which was also observed in Cu-COF, indicating that Cu site promoted the CO<sub>2</sub> molecular coupling as compared to pyrrole N along with Cu-3d<sub>z<sup>2</sup></sub> orbital. Moreover, Cu-COF is distinctly different from an intensive coupling overlap between all Cu-3d and C-2p<sub>z</sub> orbital hybridization comparing with CO<sub>2</sub>-adsorbed ZnCu-COF. Similarly, the C-2p<sub>z</sub> of \*COOH intermediate in the ZnCu-COF occurred more robust (Cu-3d<sub>z<sup>2</sup></sub>)-(C-2p<sub>z</sub>) coupling interaction than that of Cu-COF and Zn-COF. The above results suggest that the Zn centers remarkably affect the orbital energy of Cu-3d, which in turn regulate the electron state re-distribution of Cu-3d orbital, and significantly change the activation of CO<sub>2</sub> molecule and \*COOH. In particular, Cu site on ZnCu-COF and Cu-COF can promote the CO<sub>2</sub> absorption and fix \*COOH intermediate stably as compared to pyrrole N site of Zn-COF. These alterations account for the enhanced selectivity toward HCOOH (ZnCu-COF and Cu-COF) and CO (Zn-COF).

According to these analyses, the conceivable CO<sub>2</sub>RR hydrogenation pathways can be ratiocinated on these COFs in Fig. 5f-h, by considering FPP or CuFPP as the CO<sub>2</sub> reduction sites; here only a portion of the porphyrin ring is drawn to exhibit the configuration of the intermediates, even though the whole COF was selected for the calculation. The different coupling strength between Cu-3d<sub>z<sup>2</sup></sub> atomic orbital and C-2p<sub>z</sub> of CO<sub>2</sub> on Cu site (ZnCu-COF, Cu-COF) as well as pyrrole N (Zn-COF) were perceived by Gibbs free energy (ΔG) values. As shown, the first-step hydrogenation of adsorbed CO<sub>2</sub> molecules, forming \*COOH intermediates, was the rate-limiting procedure for FPP or CuFPP because of the highly ΔG. ZnCu-COF showed the lowest ΔG (0.55 eV) than Cu-COF (0.78 eV) and Zn-COF (1.26 eV), indicating an easiest CO<sub>2</sub> molecular activation on ZnCu-COF scaffold. Moreover, the differentiated HCOOH conversion ability can also be attributed to the different Cu-excited orbital states, which exhibits the electron re-distribution of Cu-3d orbital, and thereby influences the orbital energy/interacting orientation of Cu-3d (d<sub>xy</sub>, d<sub>yz</sub>, d<sub>zx</sub>, d<sub>z<sup>2</sup></sub>, and d<sub>x<sup>2</sup>-y<sup>2</sup></sub>) with C-2p<sub>z</sub> orbital of HCOOH. As indicated in Fig. 5f-g, the \*HCOOH intermediate on the CuFPP core was evolved exothermically with an energy barrier of 0.43 eV on ZnCu-COF and 0.66 eV on Cu-COF, while the formation of \*CO radical was endothermic with forming ΔG(\*CO) of 0.81 eV (ZnCu-COF) and 0.96 eV (Cu-COF). Moreover, the dissociation barrier of HCOOH (ΔG(\*+HCOOH)) products was 0.36 eV on the ZnCu-COF and 0.54 eV on the Cu-COF, which was lower than that of ΔG(\*+CO) on ZnCu-COF (0.72 eV) and Cu-COF (0.85 eV). These calculated results imply that the contained Cu single-atom sites on the COF matrix are more beneficial for \*COOH protonation to produce \*HCOOH rather than the desorption of H<sub>2</sub>O molecules to evolve the \*CO intermediates. In comparison, because the ΔG(\*CO) and ΔG(\*HCOOH) of FPP cores were an exothermal barrier (0.81 eV) and endothermal one (1.56 eV), the FPP cores tended to form CO gas by protonating \*COOH-to-\*CO with H<sub>2</sub>O molecular desorption. Possibly, the excited Cu atoms at pentafluorophenyl-porphyrin center make for promoting nucleophilic reaction between proton (\*H) and the unsaturated carbon of \*COOH, because of strong (Cu-3d<sub>z<sup>2</sup></sub>)-(C-2p<sub>z</sub>) coupling, thereby changing the photoreaction pathways to form HCOOH instead of CO in the Cu-COF and ZnCu-COF, compared to Zn-COF [59,60].

Based on the aforementioned results, the superior CO<sub>2</sub>RR performance of the ZnCu-COF with HCOOH selectivity can be associated with its unique structure. The AB-stacked frameworks exhibit a periodic array of multiple photo and catalytic centers. Therefore, compared to the traditional materials, energy transfer and electron diffusion within the

ZnCu-COF matrix would occur from ZnPP to CuFPP compartments. The enriched charge of Cu atom remarkably affects the orbital energy of Cu-3d, further deciding the electron state dispersion of Cu-3d orbital under the excited state. By manipulating the interacting orientation of Cu-3d (d<sub>xy</sub>, d<sub>yz</sub>, d<sub>zx</sub>, d<sub>z<sup>2</sup></sub>, and d<sub>x<sup>2</sup>-y<sup>2</sup></sub>) with C-2p<sub>z</sub> orbital of CO<sub>2</sub> or HCOOH, Cu site on ZnCu-COF, serving as single atom sites, promote CO<sub>2</sub> uptake and nucleophilic reaction of the unsaturated carbon of \*COOH, instead of the desorption H<sub>2</sub>O molecules to evolve \*CO intermediates, giving rise to a high HCOOH selectivity of ZnCu-COF than that of Cu-COF and Zn-COF.

#### 4. Conclusion

In summary, novel binuclear self-assembled ZnCu-COF matrices were engineered as new PMD-like heterogeneous catalysts to bridge multiple photosensitizers and catalytic cores. The ZnCu-COF matrices exhibited an average HCOOH/CO/H<sub>2</sub> yields of 138.6/12.7/4.3 μmol g<sup>-1</sup> h<sup>-1</sup> with superior 89.1% HCOOH selectivity, which is better than that of the Zn-COF and Cu-COF counterparts. Photoelectrochemical and in-suit characterizations show that the excellent photocatalytic performance is attributed to the efficient intraskeletal charge transfer via a synergistic effect of the rich Zn/Cu compartments. DTF calculation reveal that the directional and stepwise electron transfer from Zn photocenters remarkably affects the orbital energy of Cu-3d, further leading to the electron state re-distribution of Cu-3d (d<sub>xy</sub>, d<sub>zx</sub>, d<sub>yz</sub>, d<sub>z<sup>2</sup></sub>, and d<sub>x<sup>2</sup>-y<sup>2</sup></sub>) orbital. By a strong (Cu-3d<sub>z<sup>2</sup></sub>)-(C-2p<sub>z</sub>) orbital coupling, Cu centers show a lower energy barrier for CO<sub>2</sub> activation and conversion of \*COOH intermediate, which further explains how the heterobimetallic atom site affect the photocatalysis process of CO<sub>2</sub>RR in these COFs. Therefore, by a heterogenization strategy incorporating light-harvesting and catalytic molecules into COF matrices to create an artificial microenvironment with the functional and structural superiority of natural photosystems, this work offers a significant insight to regulate reaction pathway on basis of manipulating metal atom orbital state in various photoconversion reactions (CO<sub>2</sub> reduction, hydrogen production, nitrogen fixation, etc.).

#### CRedit authorship contribution statement

**Jin Ming Wang:** Conceptualization, Investigation, Methodology, Data curation, Formal analysis, Writing – original draft, **Jeong Heon Lee:** Investigation, Methodology, **Je Hee Lee:** Data curation, Formal analysis, **Tae Gyun Woo:** Data curation, Formal analysis, **Yue Xing Zhang:** Methodology, Data curation, **Woo Dong Jang:** Methodology, Validation, Data curation, **Tae Kyu Kim:** Conceptualization, Validation, Writing – review & editing.

#### Declaration of Competing Interest

The authors declare the following financial interests/personal relationships which may be considered as potential competing interests, Tae Kyu Kim reports financial support was provided by National Research Foundation of Korea.

#### Data availability

Data will be made available on request.

#### Acknowledgments

This work was supported by the National Research Foundation of Korea (NRF) grants funded by the Ministry of Education and Ministry of Science and ICT (2020R1A4A1017737, 2020R1A2C3004520, and 2022R1A2C3003081).

## Supplementary material

Supplementary material related to this article are available free of charge via the internet. Experimental details about sample preparations, material characterization, Uv-vis absorption spectra, MALDI-TOF mass spectrum, FTIR spectra, Raman spectra, Solid-state  $^{13}\text{C}$  NMR spectra,  $\text{N}_2$  adsorption-desorption isotherms, Thermogravimetric curves, and other results of measurements.

## Appendix A. Supporting information

Supplementary data associated with this article can be found in the online version at doi:10.1016/j.apcatb.2022.122287.

## References

- [1] E.J. Kim, R.L. Siegelman, H.Z.H. Jiang, A.C. Forse, J.H. Lee, J.D. Martell, P. J. Milner, J.M. Falkowski, J.B. Neaton, J.A. Reimer, S.C. Weston, J.R. Long, Cooperative carbon capture and steam regeneration with tetraamine-appended metal-organic frameworks, *Science* 369 (2020) 392–396.
- [2] X.M. Hu, K. Daasbjerg, Carbon dioxide efficiently converted to methanol, *Nature* 575 (2019) 598–599.
- [3] Y.S. Zhou, Z.T. Wang, L. Huang, S. Zaman, K. Lei, T. Yue, Z.A. Li, B. You, B.Y. Xia, Engineering 2D photocatalysts toward carbon dioxide reduction, *Adv. Energy Mater.* 11 (2021) 2003159.
- [4] Y.H. Cao, L. Guo, M. Dan, D.E. Doronkin, C.Q. Han, Z.Q. Rao, Y. Liu, J. Meng, Z. A. Huang, K.B. Zheng, P. Chen, F. Dong, Y. Zhou, Modulating electron density of vacancy site by single Au atom for effective  $\text{CO}_2$  photoreduction, *Nat. Commun.* 12 (2021) 1675.
- [5] A. Sabbah, I. Shown, M. Qorbani, F.Y. Fu, T.Y. Lin, H.L. Wu, P.W. Chung, C.I. Wu, S.R.M. Santiago, J.L. Shen, K.H. Chen, L.C. Chen, Boosting photocatalytic  $\text{CO}_2$  reduction in a  $\text{ZnS}/\text{ZnIn}_2\text{S}_4$  heterostructure through strain-induced direct Z-scheme and a mechanistic study of molecular  $\text{CO}_2$  interaction thereon, *Nano Energy* 93 (2022), 106809.
- [6] F.L. Wang, T.T. Hou, X. Zhao, W. Yao, R.Q. Fang, K. Shen, Y.W. Li, Ordered macroporous carbonous frameworks implanted with CdS quantum dots for efficient photocatalytic  $\text{CO}_2$  reduction, *Adv. Mater.* 33 (2021) 2102690.
- [7] J. Li, H.L. Huang, W.J. Xue, K. Sun, X.H. Song, C.R. Wu, L. Nie, Y. Li, C.Y. Liu, Y. Pan, H.L. Jiang, D.H. Mei, C.L. Zhong, Self-adaptive Dual-metal-site pairs in metal-organic frameworks for selective  $\text{CO}_2$  photoreduction to  $\text{CH}_4$ , *Nat. Catal.* 4 (2021) 719–729.
- [8] J.M. Wang, E.H. Kim, D.P. Kumar, A.P. Rangappa, Y.J. Kim, Y.X. Zhang, T.K. Kim, Highly durable and fully dispersed Co diatomic site catalysts for  $\text{CO}_2$  photoreduction to  $\text{CH}_4$ , *Angew. Chem. Int. Ed.* 61 (2022), e202113044.
- [9] J. Li, W.F. Pan, Q.Y. Liu, Z.Q. Chen, Z.J. Chen, X.Z. Feng, H. Chen, Interfacial engineering of  $\text{Bi}_{19}\text{Br}_{327}$  nanowires promotes metallic photocatalytic  $\text{CO}_2$  reduction activity under near-infrared light irradiation, *J. Am. Chem. Soc.* 143 (2021) 6551–6559.
- [10] P. Zhang, S.B. Wang, B.Y. Guan, X.W. Lou, Fabrication of CdS hierarchical multi-cavity hollow particles for efficient visible light  $\text{CO}_2$  reduction, *Energy Environ. Sci.* 12 (2019) 164–168.
- [11] Z. Jiang, X.H. Xu, Y.H. Ma, H.S. Cho, D. Ding, C. Wang, J. Wu, P. Oleynikov, M. Jia, J. Cheng, Y. Zhou, O. Terasaki, T.Y. Peng, L. Zan, H.X. Deng, Filling metal-organic framework mesopores with  $\text{TiO}_2$  for  $\text{CO}_2$  photoreduction, *Nature* 586 (2020) 549–554.
- [12] S.B. Jin, M. Supur, M. Addicoat, K. Furukawa, L. Chen, T. Nakamura, S. Fukuzumi, S. Irle, D.L. Jiang, Creation of superheterojunction polymers via direct polycondensation: Segregated and  $\pi$ -continuous donor-acceptor  $\text{Pi}$ -columnar arrays in covalent organic frameworks for long-lived charge separation, *J. Am. Chem. Soc.* 137 (2015) 7817–7827.
- [13] S. Chen, K. Li, F. Zhao, L. Zhang, M. Pan, Y.Z. Fan, J. Guo, J.Y. Shi, C.Y. Su, A Metal-organic, cage incorporating multiple light harvesting and catalytic centers for photochemical hydrogen production, *Nat. Commun.* 7 (2016) 13169.
- [14] Y.G. Hu, F. Zhan, Q. Wang, Y.J. Sun, C. Yu, X. Zhao, H. Wang, R. Long, G.Z. Zhang, C. Gao, W.K. Zhang, J.J.Y. Tao, Y.J. Xiong, Tracking mechanistic pathway of photocatalytic  $\text{CO}_2$  reaction at Ni sites using operando, time-resolved spectroscopy, *J. Am. Chem. Soc.* 142 (2020) 5618–5626.
- [15] S. Amthor, S. Knoll, M. Heiland, L. Zedler, C. Li, D. Naurooz, W. Tobiaschus, A. K. Mengele, M. Anjass, U.S. Schubert, B. Dietzek-Ivansic, S. Rau, C.A. Streh, A photosensitizer-polyoxometalate dyad that enables the decoupling of light and dark reactions for delayed on-demand solar hydrogen production, *Nat. Chem.* 14 (2022) 321–327.
- [16] G.F. Manbeck, E. Fujita, K.J. Brewer, Tetra- and heptametallic  $\text{Ru(II)}$ ,  $\text{Rh(III)}$  supramolecular hydrogen production photocatalysts, *J. Am. Chem. Soc.* 139 (2017) 7843–7854.
- [17] G.F. Li, D.X. Zhu, X.L. Wang, M.R. Bryce, Dinuclear metal complexes: Multifunctional properties and applications, *Chem. Soc. Rev.* 49 (2020) 765–838.
- [18] C. Gao, J. Wang, H.X. Xu, Y.J. Xiong, Coordination chemistry in the design of heterogeneous photocatalysts, *Chem. Soc. Rev.* 46 (2017) 2799–2823.
- [19] X.J. Lang, X.D. Chen, J.C. Zhao, Heterogeneous visible light photocatalysis for selective organic transformations, *Chem. Soc. Rev.* 43 (2014) 473–486.
- [20] S. Berardi, S. Drouet, L. Francas, C. Gimbert-Surinach, M. Guttentag, C. Richmond, T. Stoll, A. Llobet, Molecular artificial photosynthesis, *Chem. Soc. Rev.* 43 (2014) 7501–7519.
- [21] H.Y. Jiang, P. Zhou, Y. Wang, R. Duan, C. Chen, W. Song, J. Zhao, Copper-based coordination polymer nanostructure for visible light photocatalysis, *Adv. Mater.* 28 (2016) 9776–9781.
- [22] M. Zhang, M. Lu, Z.L. Lang, J. Liu, M. Liu, J.N. Chang, L.Y. Li, L.J. Shang, M. Wang, S.L. Li, Y.Q. Lan, Semiconductor/covalent-organic-framework Z-scheme heterojunctions for artificial photosynthesis, *Angew. Chem. Int. Ed.* 59 (2020) 6500–6506.
- [23] Y.M. Huang, P.Y. Du, W.X. Shi, Y. Wang, S. Yao, Z.M. Zhang, T.B. Lu, X.Q. Lu, Filling COFs with bimetallic nanoclusters for  $\text{CO}_2$ -to-alcohols conversion with  $\text{H}_2\text{O}$  oxidation, *Appl. Catal. B* 288 (2021), 120001.
- [24] H.S. Lu, W.K. Han, X. Yan, C.J. Chen, T. Niu, Z.G. Gu, A 3D anionic metal covalent organic framework with soc topology built from an octahedral  $\text{Ti(IV)}$  complex for photocatalytic reactions, *Angew. Chem. Int. Ed.* 60 (2021) 17881–17886.
- [25] N. Huang, X. Chen, R. Krishna, D.L. Jiang, Two-dimensional covalent organic frameworks for carbon dioxide capture through channel-wall functionalization, *Angew. Chem. Int. Ed.* 54 (2015) 2986–2990.
- [26] Y. Yue, P.Y. Cai, K. Xu, H.Y. Li, H.Z. Chen, H.C. Zhou, N. Huang, Stable bimetallic polyphthalocyanine covalent organic frameworks as superior electrocatalysts, *J. Am. Chem. Soc.* 143 (2021) 18052–18060.
- [27] E.X. Chen, M. Qiu, Y.F. Zhang, Y.S. Zhu, L.Y. Liu, Y.Y. Sun, X.H. Bu, J. Zhang, Q. Lin, Acid and base resistant zirconium polyphenolate-metalloporphyrin scaffolds for efficient  $\text{CO}_2$  photoreduction, *Adv. Mater.* 30 (2018) 1704388.
- [28] W.B. Liu, X.K. Li, C.M. Wang, H.H. Pan, W.P. Liu, K. Wang, Q.D. Zeng, R.M. Wang, J.Z. Jiang, A scalable general synthetic approach toward ultrathin imine-linked two-dimensional covalent organic framework nanosheets for photocatalytic  $\text{CO}_2$  Reduct., *J. Am. Chem. Soc.* 141 (2019) 17431–17440.
- [29] N.Y. Huang, H. He, S. Liu, H.L. Zhu, Y.J. Li, J. Xu, J.R. Huang, X. Wang, P.Q. Liao, X.M. Chen, Electrostatic attraction-driven assembly of a metal-organic framework with a photosensitizer boosts photocatalytic  $\text{CO}_2$  reduction to CO, *J. Am. Chem. Soc.* 143 (2021) 17424–17430.
- [30] D.L. Meng, M.D. Zhang, D.H. Si, M.J. Mao, Y. Hou, Y.B. Huang, R. Cao, Highly selective tandem electroreduction of  $\text{CO}_2$  to ethylene over atomically isolated nickel–nitrogen site/copper nanoparticle catalysts, *Angew. Chem. Int. Ed.* 60 (2021) 25485–25492.
- [31] G.X. Yang, C.X. Lin, X.N. Feng, T.Y. Wang, J.Z. Jiang, Multi-component supramolecular gels induce protonation of a porphyrin exciplex to achieve improved collective optical properties for effective photocatalytic hydrogen generation, *Chem. Commun.* 56 (2020) 527–530.
- [32] L. Chen, Y. Yang, D.L. Jiang, CMPs as scaffolds for constructing porous catalytic frameworks: A built-in heterogeneous catalyst with high activity and selectivity based on nanoporous metalloporphyrin polymers, *J. Am. Chem. Soc.* 132 (2010) 9138–9143.
- [33] Y. Meng, Y. Luo, J.L. Shi, H.M. Ding, X. Lang, W. Chen, A.M. Zheng, J.L. Sun, C. Wang, 2D and 3D porphyrinic covalent organic frameworks: The influence of dimensionality on functionality, *Angew. Chem. Int. Ed.* 59 (2020) 3653–3658.
- [34] R.F. Chen, J.L. Shi, Y. Ma, G.Q. Lin, X.J. Lang, C. Wang, Designed synthesis of a 2D porphyrin-based  $\text{sp}^2$  carbon-conjugated covalent organic framework for heterogeneous photocatalysis, *Angew. Chem. Int. Ed.* 58 (2019) 6430–6434.
- [35] S.Z. Yang, W.H. Hu, X. Zhang, P.L. He, B. Pattengale, C. Liu, M. Cendejas, I. Hermans, X.Y. Zhang, J. Zhang, J.E. Huang, 2D covalent organic frameworks as intrinsic photocatalysts for visible light-driven  $\text{CO}_2$  reduction, *J. Am. Chem. Soc.* 140 (2018) 14614–14618.
- [36] X.H. He, Q. He, Y.C. Deng, M. Peng, H.Y. Chen, Y. Zhang, S.Y. Yao, M.T. Zhang, D. Q. Xiao, D. Ma, B.H. Ge, H.B. Ji, A versatile route to fabricate single atom catalysts with high chemoselectivity and regioselectivity in hydrogenation, *Nat. Commun.* 10 (2019) 3663.
- [37] Y. Kuramochi, Y. Fujisawa, A. Satake, Photocatalytic  $\text{CO}_2$  reduction mediated by electron transfer via the excited triplet state of  $\text{Zn(II)}$  porphyrin, *J. Am. Chem. Soc.* 142 (2020) 705–709.
- [38] Y.B. Ding, W.H. Zhu, Y.S. Xie, Development of ion chemosensors based on porphyrin analogues, *Chem. Rev.* 117 (2017) 2203–2256.
- [39] Q.P. Lin, J.Z. Lu, Z.D. Yang, X.C. Zeng, J. Zhang, Porphyrinic porous organic frameworks: Preparation and post-synthetic modification via demetallation–remetallation, *J. Mater. Chem. A* 2 (2014) 14876–14882.
- [40] Z.M. Liu, I. Schmidt, P. Thamyongkit, R.S. Loewe, D. Syomin, J.R. Diers, Q. Zhao, V. Misra, J.S. Lindsey, D.F. Bocian, Synthesis and film-forming properties of ethynylporphyrins, *Chem. Mater.* 17 (2005) 3728–3742.
- [41] L. Chen, Y. Yang, D.L. Jiang, CMPs as scaffolds for constructing porous catalytic frameworks: A built-in heterogeneous catalyst with high activity and selectivity based on nanoporous metalloporphyrin polymers, *J. Am. Chem. Soc.* 132 (2010) 9138–9143.
- [42] H.X. Jia, Y.C. Yao, Y.Y. Gao, D.P. Lu, P.W. Du, Pyrolyzed cobalt porphyrin-based conjugated mesoporous polymers as bifunctional catalysts for hydrogen production and oxygen evolution in water, *Chem. Commun.* 52 (2016) 13483–13486.
- [43] P.D. Rao, B.J. Littler, G.R. Geier, J.S. Lindsey, Efficient synthesis of monoacyl dipyrromethanes and their use in the preparation of sterically unhindered trans-porphyrins, *J. Org. Chem.* 65 (2000) 1084–1092.
- [44] J.M. Wang, J. Luo, D. Liu, S.T. Chen, T.Y. Peng, One-pot solvothermal synthesis of  $\text{MoS}_2$ -modified  $\text{Mn}_{0.2}\text{Cd}_{0.8}\text{S}/\text{MnS}$  heterojunction photocatalysts for highly efficient visible-light-driven  $\text{H}_2$  production, *Appl. Catal. B* 241 (2019) 130–140.
- [45] W. Wang, C.Y. Deng, S.J. Xie, Y.F. Li, W.Y. Zhang, H. Sheng, C.C. Chen, J.C. Zhao, Photocatalytic C-C coupling from carbon dioxide reduction on copper oxide with mixed-valence Copper(I)/Copper(II), *J. Am. Chem. Soc.* 143 (2021) 2984–2993.

- [46] R.F. Chen, Y. Wang, Y. Ma, A. Mal, X.Y. Gao, L. Gao, L.J. Qiao, X.B. Li, L.Z. Wu, C. Wang, Rational design of isostructural 2D porphyrin-based covalent organic frameworks for tunable photocatalytic hydrogen evolution, *Nat. Commun.* 12 (2021) 1354.
- [47] T.X. Wang, L.L. Guo, Z. Jiang, S.T. Chen, S.R. Xu, Y.X. Zhang, J. Zhang, R.J. Li, T. Y. Peng, Ru-pincer complex-bridged Cu-porphyrin polymer for robust (photo) electrocatalytic H<sub>2</sub> evolution via single-atom active sites, *Adv. Funct. Mater.* 31 (2021) 2107290.
- [48] J.M. Wang, M.T. Kuo, P. Zeng, L. Xu, S.T. Chen, T.Y. Peng, Few-layer BiVO<sub>4</sub> nanosheets decorated with SrTiO<sub>3</sub>: Rh nanoparticles for highly efficient visible-light-driven overall water splitting, *Appl. Catal. B* 279 (2020), 119377.
- [49] K. Li, B.S. Peng, T.Y. Peng, Recent advances in heterogeneous photocatalytic CO<sub>2</sub> conversion to solar fuels, *ACS Catal.* 6 (2016) 7485–7527.
- [50] A. Weu, R. Kumar, J.F. Butscher, V. Lami, F. Paulus, A.A. Bakulin, Y. Yaynzof, Unveiling the activity origin of iron nitride as catalytic material for efficient hydrogenation of CO<sub>2</sub> to C<sub>2+</sub> hydrocarbons, *Angew. Chem. Int. Ed.* 60 (2021) 4496–4500.
- [51] C. Cheng, B.W. He, J.J. Fan, B. Cheng, S.W. Cao, J.G. Yu, Facile top-down strategy for direct metal atomization and coordination achieving a high turnover number in CO<sub>2</sub>, *Photo. J. Am. Chem. Soc.* 142 (2020) 19259–19267.
- [52] J.C. Zhu, W.W. Shao, X.D. Li, X.C. Jiao, J.F. Zhu, Y.F. Sun, Y. Xie, Asymmetric triple-atom sites confined in ternary oxide enabling selective CO<sub>2</sub> photothermal reduction to acetate, *J. Am. Chem. Soc.* 143 (2021) 18233–18241.
- [53] H.N. Shi, H.Z. Wang, Y.C. Zhou, J.H. Li, P.L. Zhai, X.Y. Li, G.G. Gurzadyan, J. G. Hou, H. Yang, X.W. Guo, Atomically dispersed indium-copper dual-metal active sites promoting C-C coupling for CO<sub>2</sub> photoreduction to ethanol, *Angew. Chem. Int. Ed.* 61 (2022), e202208904.
- [54] A. Weu, R. Kumar, J.F. Butscher, V. Lami, F. Paulus, A.A. Bakulin, Y. Yaynzof, Energy transfer to a stable donor suppresses degradation in organic solar cells, *Adv. Funct. Mater.* 30 (2019) 1907432.
- [55] C. Cheng, B.W. He, J.J. Fan, B. Cheng, S.W. Cao, J.G. Yu, An inorganic/organic S-scheme heterojunction H<sub>2</sub>-production photocatalyst and its charge transfer mechanism, *Adv. Mater.* 33 (2021), e2100317.
- [56] S.C. Lin, C.C. Chang, S.Y. Chiu, H.T. Pai, T.Y. Liao, C.S. Hsu, W.H. Chiang, M. K. Tsai, H.M. Chen, Operando time-resolved X-ray absorption spectroscopy reveals the chemical nature enabling highly selective CO<sub>2</sub> reduction, *Nat. Commun.* 11 (2020) 3525.
- [57] B.H. Zhao, M.Y. Sun, F.P. Chen, Y.M. Shi, Y.F. Yu, X.G. Li, B. Zhang, UV-photochemistry of the disulfide bond: Evolution of early photoproducts from picosecond X-ray absorption spectroscopy at the sulfur K-edge, *J. Am. Chem. Soc.* 140 (2018) 6554–6561.
- [58] A.A. Cordones, J.H. Lee, K. Hong, H. Cho, K. Garg, M. Boggio-Pasqua, J.J. Rack, N. Huse, R.W. Schoenlein, T.K. Kim, Transient metal-centered states mediate isomerization of a photochromic ruthenium-sulfoxide complex, *Nat. Commun.* 9 (2018) 1989.
- [59] B. Wei, Y.S. Xiong, Z.Y. Zhang, J.H. Hao, L.H. Li, W.D. Shi, Efficient electrocatalytic reduction of CO<sub>2</sub> to HCOOH by bimetallic In-Cu nanoparticles with controlled growth facet, *Appl. Catal. B* 283 (2021), 119646.
- [60] W.Y. Zhang, Y.G. Chao, W.S. Zhang, J.H. Zhou, F. Lv, K. Wang, F.X. Lin, H. Luo, J. Li, M.P. Tong, E.K. Wang, S.J. Guo, Emerging dual-atomic-site catalysts for efficient energy catalysis, *Adv. Mater.* 33 (2021) 2102576.